INTERNATIONAL JOURNAL FOR NUMERICAL METHODS IN BIOMEDICAL ENGINEERING
Int. J. Numer. Meth. Biomed. Engng. 2012; **28**:678–696
Published online 17 January 2012 in Wiley Online Library (wileyonlinelibrary.com). DOI: 10.1002/cnm.1488

Modeling shear waves through a viscoelastic medium induced by acoustic radiation force

Kristen H. Lee [1], Benjamin A. Szajewski [1], Zaegyoo Hah [2], Kevin J. Parker [2] and Antoinette M. Maniatty [1,*,†]

[1] *Department of Mechanical, Aerospace, and Nuclear Engineering, Rensselaer Polytechnic Institute, Troy, New York 12180, USA*
[2] *Department of Electrical and Computer Engineering, University of Rochester, Rochester, New York 14627, USA*

SUMMARY

In this study, a finite element model of a tissue-mimicking, viscoelastic phantom with a stiffer cylindrical inclusion subjected to an acoustic radiation force (ARF) is presented, and the resulting shear waves through the heterogeneous media are simulated, analyzed, and compared with experimental data. Six different models for the ARF were considered and compared. Each study used the same finite element model, but applied the following: (1) full radiation push; (2) focal region push; (3) single element focal point source; or (4) various thresholds of the full radiation push. For each case, displacements at discrete locations were determined and compared. The finite element simulation results for the full radiation push matched well with the experimental data with respect to replicating the shear wave speed and attenuation in the peak displacements through the background medium and inclusion, but did not illustrate comparable recovery after the peak displacements. As a result of this study, it has been shown that a focal region or point source push is not adequate to accurately model the effects of the full radiation push, but thresholding the full push can produce comparable results and reduce computation time. Copyright © 2012 John Wiley & Sons, Ltd.

Received 1 June 2011; Revised 11 October 2011; Accepted 3 November 2011

KEY WORDS: elastography; viscoelasticity; shear waves; acoustic radiation force

1. INTRODUCTION

The use of palpation to determine the health of soft tissue has been a historical practice that is still used at present in clinical exams. Although effective, palpation may not be able to detect tumors that are deep within the soft tissue. In the past two decades, there has been significant investigation into the possible use of remote palpation techniques, which provide non-invasive means of determining tissue health. The primary aim of these techniques is to quantitatively estimate and image biomechanical properties that are associated with the tissue structure and pathology, such as the shear modulus, for diagnosis. The biomechanical properties may be estimated using inverse methods applied to tissue displacement measurements, such as those described in [1–3]. The tissue displacements may result from a static [4] or dynamic load [5], and the load may be applied through either external mechanical means [6] or by creating an acoustic radiation force (ARF) from a focused ultrasound transducer [7]. The displacements may be measured using either ultrasound imaging or MRI [8, 9]. Both modalities have shown potential for clinical use [7, 10, 11], with ultrasound being lower in cost, but MRI being able to image regions, such

*Correspondence to: Antoinette M. Maniatty, Department of Mechanical, Aerospace, and Nuclear Engineering, Rensselaer Polytechnic Institute,110 8th Street, Troy, New York 12180, USA.
†E-mail: maniaa@rpi.edu

as the brain, that are inaccessible with ultrasound. This work focuses on the dynamic response of soft tissue to ARF, and presents simulation tools for modeling the tissue response to correlate with experimental observations.

Ultrasonic techniques have been used to image displacements in soft tissue resulting from dynamic excitations that generate shear waves with the goal of identifying elastic and viscoelastic properties that affect the wave speed, amplitude, phase, and attenuation. Sarvazyan *et al*. [5] proposed a method they called shear wave elasticity imaging that uses the highly localized application of radiation force from focused ultrasound to characterize soft tissue. One of the challenges in using ultrasound to image shear waves is the relatively fast speed of the wave compared with the standard ultrasound scanner frame rate. To overcome this limitation, Fink and co-workers developed an ultrafast, ultrasonic imaging system that can be used to measure one or two components of the displacement field as a function of time on an imaging plane associated with propagating shear waves [6, 12, 13]. In that work, they used two methods to generate the shear waves, which they refer to as transient elastography and supersonic shear imaging. In transient elastography, an external mechanical source with a single pulse induces a traveling shear wave in the tissue, which can be imaged as a function of time within the medium. supersonic shear imaging utilizes an ultrasound transducer to induce shear waves through a fast sequence of acoustic radiation pushes along a line, which create shear waves that constructively interfere and can be imaged with the ultrafast, ultrasonic scanner. By utilizing an ARF generated from an ultrasonic transducer, it is possible to induce displacements deep within the tissue. In 2001, Nightingale *et al*. [7] demonstrated the feasibility of using ARF as a technique for remote palpation. In that work, local tissue stiffness was associated with the magnitude of the tissue displacement, which was induced by the ARF. Nightingale *et al*. [14] also demonstrated the feasibility for acoustic radiation force imaging (ARFI) with *in vivo* and *ex vivo* experiments. In this ARFI method, transient shear waves were generated using ARF, and their propagation was visualized with the ultrasound transducer. The shear wave speed was estimated from the slope of the edge of the first wave through time and used to compute the local shear modulus. Multiple experiments were performed to acquire data at different times after the ARF push. Chen *et al*. [15] developed shearwave dispersion ultrasound vibrometry (SDUV), where both elasticity and viscosity measurements are determined from the frequency dispersion of the shear wave propagation speed. The shear wave propagation speed was determined by tracking the phase change of the wave produced by an ARF.

Sonoelastographic imaging, developed by Parker and co-workers [8], utilizes the vibration patterns created by the low-frequency propagation of shear waves at low depths in soft tissue. The advantage of this method is that conventional ultrasound scanners may be used to image the harmonic tissue motion. The vibration amplitude and phase can then be estimated using conventional Doppler techniques. Wu *et al*. [16] used this method to estimate the shear velocity distribution for soft tissue in a technique utilizing *crawling waves*. In this method, crawling waves is the term used to describe the motion of the interference patterns that are created when two sources vibrate at slightly different frequencies. Crawling waves are advantageous because the method is compatible with conventional Doppler imaging scanners and is practical for clinical use in estimating elasticity properties of breast, prostate, liver, and thyroid tissues. Wu *et al*. also demonstrated that the shear wave velocity of the propagating wave was approximately proportional to the interference pattern speed in certain cases. Lin *et al*. [17] developed an inverse method to image the shear wave speed from the crawling wave data. Using the concept of crawling waves, Hah *et al*. [18] developed a method to create these waves using radiation force excitation. It is this last experiment that motivates the work presented here.

There have been prior efforts to model the response of soft tissue to an ARF excitation to interpret and corroborate experimental studies. In those works, different approaches have been taken to modeling the ARF. For example, in Bercoff *et al*. [19], the full push of the ARF is considered, in Palmeri *et al*. [20], a portion of the ARF field, determined by a threshold of the maximum intensity, is used, in Vappou *et al*. [21], the force is applied at only selected elements near the focus, and in Giannoula *et al*. [22], a point source at the focus is used. This work will determine whether or not a point source or a push in a small region near the focus is sufficient to adequately replicate experimental data, or if the full push is required. Thresholding the full push is also investigated

DOI: 10.1002/cnm

to determine if a percentage of the maximum body force (or intensity) may be used to accurately represent the experimental data while reducing the computation time.

This work presents a method for three-dimensional (3D) modeling of heterogeneous viscoelastic material in response to an ARF. In Bercoff *et al*. [19], a Green's function approach is used to model the response of a viscoelastic material to an ARF, which is limited to infinite, homogeneous materials. Bercoff *et al*. touched upon the topic of only using a focal point source rather than the full field; however, only the response at a single location was observed, so the full effect on the shear wave was not investigated. This work also utilizes a Generalized Maxwell viscoelastic model instead of the Voigt model, which was used by Bercoff *et al*. and Giannoula *et al*. [19, 22]. The Generalized Maxwell model is more physically realistic than the Voigt model as it accounts for relaxation over a range of frequencies and does not predict an infinite wave speed at infinite frequency, which is associated with the speed of the wave front. In comparison with the 3Dfinite element model presented in Palmeri *et al*. [20], this work considers a viscoelastic material rather than a purely elastic material. Furthermore, in this work, a higher order integration scheme for computing the force near the focus is used to allow for a coarser discretization near the focus improving efficiency while maintaining accuracy. Both studies, however, utilize the Field II software, created by Jensen [23, 24], to compute the radiation intensity field. Vappou *et al*. [21] used ABAQUS (ABAQUS Inc., Providence, RI, USA) [25] to model the viscoelastic material, as in the current work; although the radiation force is simulated only in the focal region of the model, not the full field, and a homogeneous viscoelastic material was considered. Lastly, Giannoula *et al*. presented a finite element model of the shear waves propagating through a heterogeneous viscoelastic material, but was only two-dimensional (2D) and the excitation was implemented only at the focus.

In this work, simulation tools for modeling the shear waves resulting from an ARF excitation are developed. The ultimate goals of the simulations described here are as follows:

1. To assist experimental design work by providing a predictive model for given transducer settings and experimental setup and conditions;
2. To correlate theoretical and experimental results and provide insight on experimental observations;
3. To provide quantitative data to test inverse algorithms for reconstructing the viscoelastic properties of soft tissue; and
4. To set a framework for future finite element models that may incorporate additional experimental features.

The organization of this paper is as follows. In Section 2, the theoretical framework of this work is provided, including the constitutive equations for the selected rheological model and the mathematical model for the ARF. In Section 3, the developed finite element model and simulation methods are described, including an explanation of the case studies performed in this work. The experimental set-up that is modeled and used for calibrating and testing the model is also described here. In Section 4, the displacement fields from the finite element simulations are presented and stepped through time to illustrate the propagating shear waves for each case study. The simulation nodal displacement plots as a function of time are also presented and compared with experimental data. Finally, in Sections 5 and 6, the results are discussed and a brief conclusion of the overall work is provided.

2. THEORY

In this section, the theoretical framework for the work is provided. The governing equations used to describe the behavior of viscoelastic materials is presented. In addition to the material framework, the equations relating the acoustic radiation force to the radiation intensity are provided.

2.1. Viscoelastic Material Model

The behavior of the soft tissue is represented by an isotropic, Generalized Maxwell two-element viscoelastic model illustrated in Figure 1. In this model, μ_∞ is the long-term shear modulus, μ_1 and

DOI: 10.1002/cnm

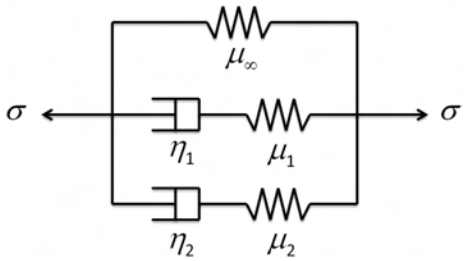

Figure 1. Generalized Maxwell two-element viscoelastic model.

μ_2 are the shear moduli for Maxwell elements 1 and 2, respectively, and η_1 and η_2 are the viscosities for elements 1 and 2, respectively. Decomposing the stress tensor, σ_{ij} into volumetric and deviatoric parts (using standard indicial notation [26, 27]) results in

$$\sigma_{ij} = \sigma'_{ij} - p\delta_{ij} \tag{1}$$

In this expression, σ'_{ij} is the deviatoric stress, p is the pressure associated with the volumetric stress, and δ_{ij} is the Kronecker delta. In this work, the deviatoric behavior is treated as viscoelastic, whereas the volumetric part is treated as linear elastic with

$$p = -\sigma_{kk} = -K\varepsilon_{kk} \tag{2}$$

where K is the bulk modulus and ε_{kk} is the trace of the strain tensor. The viscoelastic, deviatoric behavior, as represented in the model in Figure 1, is defined by the relationships

$$\sigma'_{ij} = \sigma'^{\infty}_{ij} + \sigma'^{(1)}_{ij} + \sigma'^{(2)}_{ij} \tag{3}$$

$$\sigma'^{\infty}_{ij} = \mu_\infty \varepsilon'_{ij} \tag{4}$$

$$\sigma'^{(m)}_{ij} = \mu_m \varepsilon'^{e(m)}_{ij} = \eta_m \frac{\mathrm{d}\varepsilon'^{v(m)}_{ij}}{\mathrm{d}t} \tag{5}$$

$$\varepsilon'_{ij} = \varepsilon'^{v(m)}_{ij} + \varepsilon'^{e(m)}_{ij} = \varepsilon_{ij} - \varepsilon_{kk}\delta_{ij} \tag{6}$$

where $m = 1, 2$ indicates the Maxwell element, and superscripts v and e indicate the parts of the strain acting over the viscous and elastic elements, respectively. With some manipulation, the deviatoric stress may then be expressed as a convolution integral of the form

$$\sigma'_{ij} = 2\mu_0 \int_0^t g_R(t-s) \frac{\mathrm{d}}{\mathrm{d}s}[\varepsilon'_{ij}(s)]\mathrm{d}s \tag{7}$$

where μ_0 is the instantaneous shear modulus defined as

$$\mu_0 = \mu_\infty + \mu_1 + \mu_2 \tag{8}$$

and the relaxation function $g_R(t)$ is defined as a Prony series [28],

$$g_R(t) = 1 - \sum_{m=1}^{2} g_m \left(1 - e^{-\frac{t}{\tau_m}}\right) \tag{9}$$

The parameters in the relaxation function are the relaxation time τ_m and relaxation modulus ratio g_m for each Maxwell element defined as

$$\tau_m = \frac{\eta_m}{\mu_m} \tag{10}$$

DOI: 10.1002/cnm

$$g_m = \frac{\mu_m}{\mu_0} \tag{11}$$

The two-element model is chosen here to damp out high frequency behavior, using a small relaxation time, as well as to capture observed time dependent relaxation on a larger time scale.

In addition to this isotropic, viscoelastic material behavior, the following governing equations for small strain, viscoelastic dynamics are used

$$\sigma_{ij,j} + b_i = \rho \frac{\partial^2 u_i}{\partial t^2} \tag{12}$$

$$\varepsilon_{ij} = \frac{1}{2}\left(u_{i,j} + u_{j,i}\right) \tag{13}$$

where b_i is a body force acting through the volume of the material, ρ is the density, u_i is the displacement field, and comma denotes spatial differentiation ($, j = \partial/\partial x_j$). Equation (12) is the balance of linear moment and (13) is the definition of the small strain tensor in terms of the displacement field u_i. Equations (7)–(13) together with prescribed body force field b_i (defined in the next section) and appropriate displacement and stress boundary conditions are solved for the time varying displacement field using a standard finite element method, described in Section 3.

2.2. *Acoustic radiation force*

The ARF is a body force that can be defined in terms of the temporal average acoustic intensity I_i as [5]

$$b_i = \frac{2\alpha I_i}{\rho c} \tag{14}$$

where α is the attenuation coefficient, and $c \approx \sqrt{K/\rho}$ is the sound speed in the material. The direction of the intensity is towards the focal point at locations between the transducer and the focal point (above the focal point), and the intensity is directed away from the focal point at locations below the focal point. The magnitude of the intensity vector, $\bar{I}$, is dependent upon the root mean square acoustic pressure P and the material properties of the medium according to [29]

$$\bar{I} = \frac{P^2}{2\rho c} \tag{15}$$

where the root mean square acoustic pressure is defined as the time-averaged value

$$P^2 \equiv \frac{1}{T}\int_0^T p^2 \mathrm{d}t \tag{16}$$

where T is the period between applied pushes and p is the instantaneous acoustic pressure. The expression for intensity may also be written as [30]

$$\bar{I} = \frac{P^2}{2Z} \tag{17}$$

where $Z = \rho c$ is the characteristic acoustic impedance, a property of the medium.

3. METHODS

In this section, descriptions of the experiment and model geometry, ARF model, and finite element model are given along with the simulation parameters and an explanation of the cases studied in this work.

DOI: 10.1002/cnm

3.1. Experiment and model geometry

The experiment modeled here is similar to that described in Hah *et al*. [18]. Figure 2(a) illustrates a diagram of the experimental setup. A linear transducer with a total of 192 elements was used to generate an ARF into a gelatin phantom. The transducer is centered above the inclusion so that ARF pushes on either side of the inclusion can be made by changing the set of transducer elements and focal point. In this case, the ARF was created using 124 transducer elements, for a length of approximately 25 mm, on the left-most side of the transducer to create a push on the left side of the inclusion as shown. The focal depth was 25 mm for an f-number of 1. The element height is 5 mm. The gelatin phantom contains a stiffer 6 mm cylindrical inclusion located 9.33 mm to the right and 4 mm below the ultrasonic transducer focal point. The total depth of the phantom was approximately 95 mm. As can be seen in Figure 2(a), the focal point was not exactly centered below the active elements, so the beam was slightly steered. A 250-μs pulse was created by 1250 cycles at a 5 MHz center frequency. The induced shear waves propagate through the tissue and inclusion. The transducer was then used to image the resulting displacements in the z direction with time on the center plane at a sampling rate of 2500 Hz. The displacement was imaged on a 31×301 grid (lateral by depth) with a spacing of $\Delta x = 0.6$ mm in the lateral direction and $\Delta z = 0.077$ mm in the depth direction. Defining the origin at the transducer directly above the focus, the measurements in the lateral direction were made over the range $0 \leqslant x \leqslant 18$ mm and in the depth direction over the range $11.55 \leqslant z \leqslant 34.65$ mm.

An approximate, 3D model of the experiment has been created using the commercial finite element code Abaqus [25]. A 2D diagram showing the model domain on the image plane is shown in Figure 2(b) to compare with the experiment. The model of the ARF excitation was approximated as symmetric by effectively moving the transducer 2.43 mm to the left. This was carried out to so that the dotted line bounding the model domain on the left, at $x = 0$ mm, could be approximated as a symmetry plane, reducing the size of the model. Thus, in addition to not capturing the real beam steering, the model also effectively had a symmetric inclusion on the left side of the ARF, which does not affect the results much because the reflected wave from the inclusion was largely damped out by the time it reached the model domain boundary. The full 95 mm depth of the model was

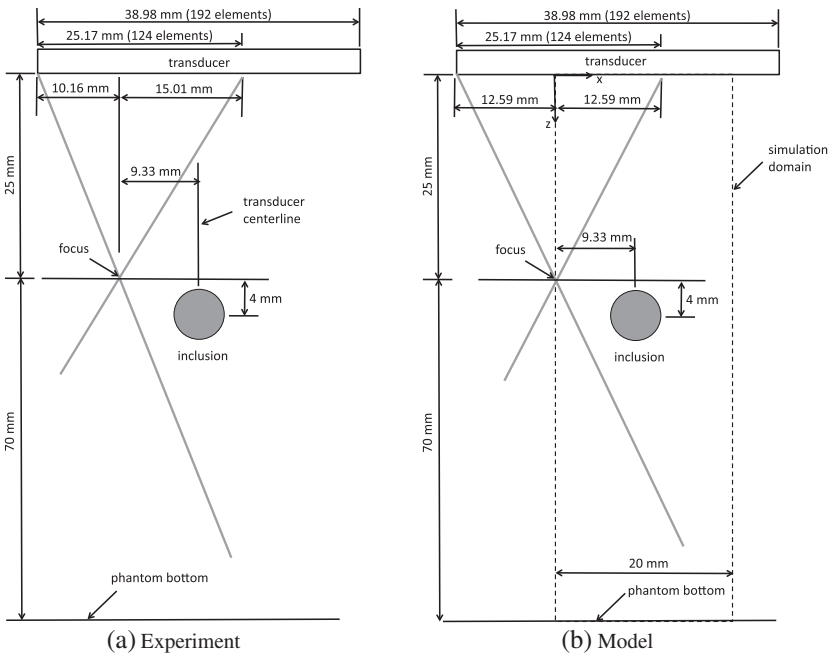

Figure 2. (a) Diagram of experimental setup and (b) approximate model of experiment assuming symmetry of acoustic intensity field. Dimensions not to scale.

DOI: 10.1002/cnm

considered, and the model was cropped on the right side at $x = 20$ mm. The model extends 10 mm in the elevation direction from the image plane. The full 3D model domain is shown in Figure 3 where the boundary conditions on each face are given.

3.2. Acoustic radiation force model

As described in Section 2.2, the applied body force resulting from the ARF may be computed from the temporal average intensity field, which is related to the acoustic pressure. The magnitude of the temporal average radiation intensity for the ultrasound transducer was computed using the pressure field obtained from the Field II Ultrasound Simulator software [23, 24]. The discretized form of Equation (16) substituted into (17) used is

$$\bar{I} = \frac{\sum_{n=1}^{N_t} p_n p_n}{2Z\lambda\omega} \tag{18}$$

where p_n is the emitted pressure at sampling time t_n, $N_t = \lambda\omega$ is the total number of sampling times, $Z = \rho c$ is the characteristic acoustic impedance, taken as 1.58×10^6 kg/(m^2 s), λ is the pulse period (time between pushes, taken as 10 ms), and ω is the sampling frequency of the pressure for computation, taken as 250 MHz. In this work, because a phantom with low attenuation is modeled, attenuation is not considered in the pressure calculation. The transducer was assumed to have a fractional bandwidth of 60%. The direction of the intensity was taken to be pointing towards the focus at every location above the focus and pointing away from the focus at every location below the focus to create an intensity vector field.

The resulting intensity field is shown in Figure 4, where the logarithm of the magnitude of the radiation intensity field normalized by the maximum intensity is imaged. On the left is a zoomed view of the region near the focus, and a single finite element near the focus is shown. Because of the large gradient in the intensity field near the focus, the intensity varies substantially within the elements near the focus. To avoid using an extremely refined mesh in this region, higher order Gaussian quadrature was used to compute an average intensity and resulting average body force in each finite element in this region. Specifically, in the *focal region*, spanning 1.2 mm laterally, 8 mm in depth, and 2.4 mm in elevation, around the 25-mm focal depth, a 10-point integration scheme (10 points in each direction, thus 1000 integration points in each element) was utilized, whereas a three-point integration scheme was used in elements outside of the focal region [31]. Using a

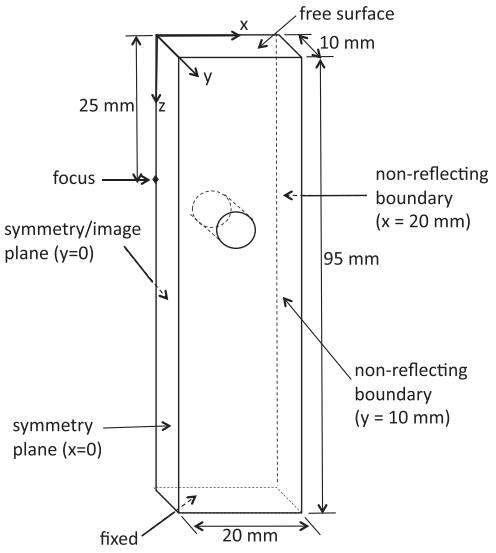

Figure 3. Three-dimensional diagram of finite element model domain showing applied boundary conditions on the faces. Dimensions not to scale.

DOI: 10.1002/cnm

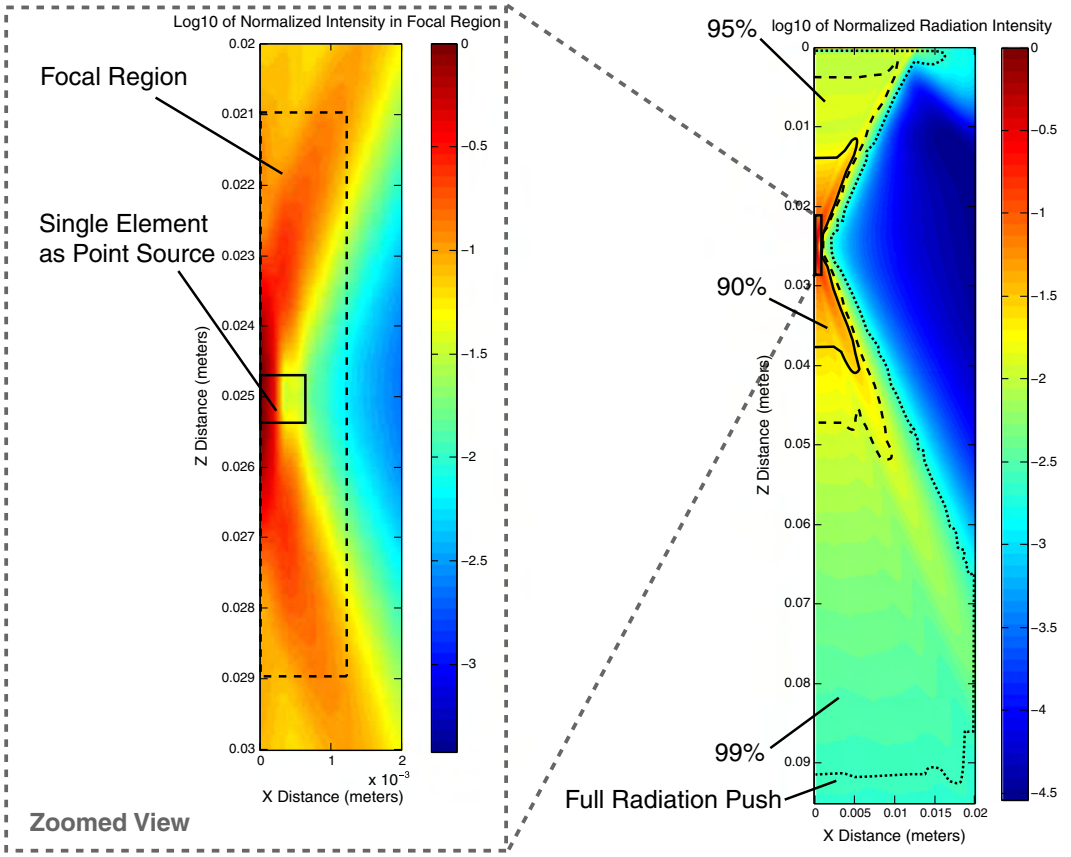

Figure 4. Logarithm of the normalized radiation intensity on the $x-z$ imaging plane with case regions outlined; percentages indicate the threshold of the maximum body force.

10-point Gauss quadrature scheme, the maximum intensity computed within the element at the focus was within 0.15% of the maximum computed intensity determined by Field II at the focus, as compared with 12.6% using the three-point scheme. Thus, the 10-point quadrature was found to adequately capture the full variation in the intensity field near the focus. Applying the Gauss quadrature numerical integration scheme [32], the average vector intensity I_i^e for each element e within the finite element model, can be calculated as

$$I_i^e = \frac{1}{\Omega^e} \sum_{q=1}^{n_{int}} I_i^q W^q J^q \tag{19}$$

where Ω^e is the volume of element e, n_{int} is the number of integration points, W^q is the integration point weight, J^q is the determinant of the Jacobian, and I_i^q is the vector intensity, for the given integration point q. The body force vector in each element, b_i^e, is then taken as proportional to this element intensity based on Equation (14)

$$b_i^e = \beta I_i^e \tag{20}$$

where β is a proportionality constant.

3.3. *Finite element model*

The model domain described in Section 3.1 was meshed with 106 993, eight-noded, linear elements with reduced integration and hourglass control, with an average element size of 0.6 mm. A mesh convergence study was performed using 1.0, 0.8, and 0.6 mm elements, and the difference in the

DOI: 10.1002/cnm

peak displacement varied by less than 5% between the 0.8 and 0.6 mm element sizes. As shown in Figure 3, symmetry boundary conditions were assumed on the vertical plane on the left side of the model ($x = 0$), which contains the focus, and on the image plane ($y = 0$). In the lateral direction on the face $x = 20$ mm and in the elevation direction on the face at $y = 10$ mm, infinite elements were used to effectively extend the domain by building in boundary damping to minimize reflections [25, 33]. Lastly, the top boundary ($z = 0$) was taken to be free, and the bottom boundary ($z = 95$ mm) was taken to be fixed in all directions. The body force was computed for each element in the finite element domain excluding the elements on the top surface at the transducer interface and in the infinite elements. Explicit, dynamic simulations were performed in Abaqus [25]. The radiation push was applied for 250 μs = 0.25 ms, as in the experiment, and the entire simulation duration was 10 ms.

Three distinct materials are considered in the model:

1. Viscoelastic background medium,
2. Viscoelastic inclusion, and
3. Elastic material in the infinite elements.

The viscoelastic material model used for the gelatin phantom background and stiffer inclusion is that presented in Section 2.1, and the infinite elements were treated as elastic. The density of all three materials was assumed to be $\rho = 1000$ kg/m^3. The shear modulus of the infinite elements was assumed to be the same as the instantaneous shear modulus μ_0 of the background. The bulk modulus K was computed from the instantaneous modulus assuming a Poisson's ratio of $\nu = 0.495$, where

$$K = \frac{2\mu(1+\nu)}{3(1-2\nu)} \tag{21}$$

A Poisson's ratio of $\nu = 0.499$ was also tested, and the results were nearly indistinguishable (less than 1.5% variation in the peak displacement). To increase the maximum allowable time step, which is limited by the ratio of the element size to the compression wave or sound speed in the material, the value of $\nu = 0.495$ was used in the simulations. By using $\nu = 0.495$ instead of 0.499, the time step could be more than doubled, because the sound speed is proportional to $\sqrt{K}$ and K is very sensitive to the Poisson's ratio when it approaches the incompressible limit of 0.5, as can be seen from Equation (21). Finally, it should be noted that a typical value of Poisson's ratio for soft tissue is $\nu = 0.49999$.

Thus, the parameters required to be identified in the model are the instantaneous shear modulus μ_0, the relaxation times τ_1 and τ_2, and the Prony series coefficients g_1 and g_2 in both the background and inclusion. The instantaneous shear modulus was determined by estimating the speed of the wave front in the background and inclusion. Because the wave front is the fastest part of the wave, it is associated with the highest frequencies, and the shear wave speed at very high frequencies tends to

$$c_s^0 = \sqrt{\frac{\mu_0}{\rho}} \tag{22}$$

Given that the excitation was created with a rectangular impulse, very high frequencies are excited, and thus, Equation (22) may be used to find μ_0. The relaxation times need to be set to damp out oscillations that may result from the 250 μs excitation as well as capture the longer relaxation time behavior after the wave passes. Thus, relaxation times in the range 10–1000 μs were considered. The Prony series coefficients must each be between zero and one, and the sum of the Prony series coefficients, g_1 and g_2, is also restricted to be such that $0 < g_1 + g_2 < 1$, based on the definition from Equations (11) and (8). Given these constraints, the material properties were determined by trial and error. On the order of 100 trials were performed comparing the simulation results against experimental measurements at select locations in the background and inclusion. Although exact replication was not achieved, the best parameters from the trials were chosen as the final material properties and are listed in Table I. Figures 5 and 6 shows a comparison of the resulting displacements in the z (depth) direction, normalized by the peak displacement at the point closest to the focus, for a set of

DOI: 10.1002/cnm

Table I. Model material properties.

Material parameter	Units	Background	Inclusion	Infinite material
μ_0	Pa	18 395	43 478	18 395
g_1	—	0.11	0.14	—
τ_1	μs	85	85	—
g_2	—	0.14	0.08	—
τ_2	μs	500	300	—

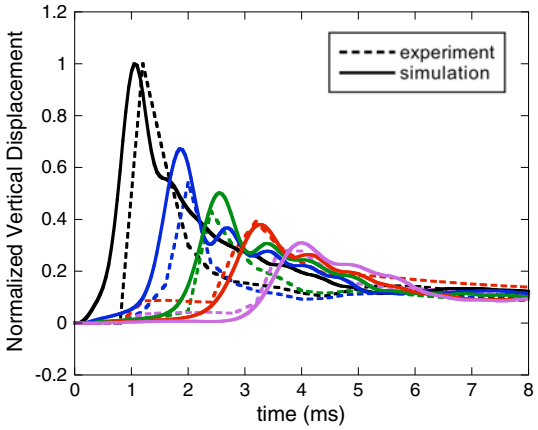

Figure 5. Comparison between experimental and simulation displacement results as a function of time using the full radiation push; for a set of points at the focal depth above the inclusion.

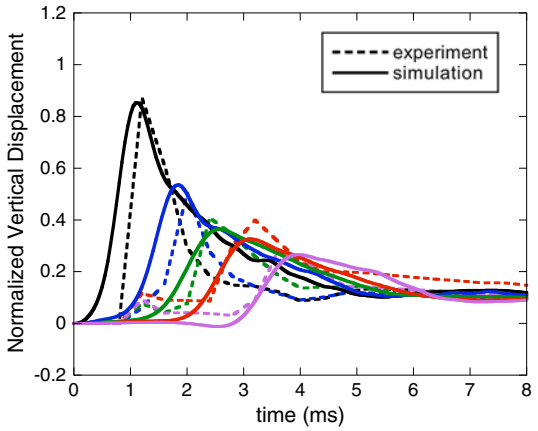

Figure 6. Comparison between experimental and simulation displacement results as a function of time using the full radiation push; for a set of points at the depth of the center of the inclusion passing through the inclusion.

10 points, five points above the inclusion at the focal depth and five points at the depth of the center of the inclusion. The locations of the points considered are illustrated in Figure 7. The root mean square difference between the measured and computed normalized displacements was found to be 0.08 for both the set of points above the inclusion and for those at the depth of the inclusion. Further discussion of these results is given in Section 5.

DOI: 10.1002/cnm

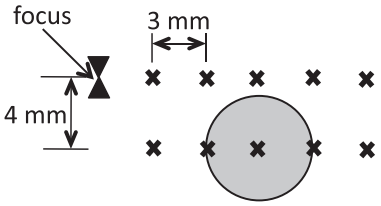

Figure 7. Location of points, marked by **x**, used in comparing experiment and simulation in Figures 5 and 6.

3.4. Case studies

Six case studies were performed to determine the effect of using a subset of the region, where the intensities are highest, to apply the ARF to induce the shear wave through the heterogeneous medium. These cases were as follows:

Case 1. Full radiation push
Case 2. Threshold the full push at 99% of the maximum body force
Case 3. Threshold the full push at 95% of the maximum body force
Case 4. Threshold the full push at 90% of the maximum body force
Case 5. Focal region push
Case 6. Single element point source push

The first case included the entire radiation field as a baseline case. Cases 2–4 used a percentage of the full radiation field to determine if thresholding would provide comparable results. Case 5 incorporated the 104 focal elements in the region defined previously. The final case used the body force from a single element to simulate a point source. The regions where the body forces are applied in each case study are shown in Figure 4, superimposed on the logarithm of the normalized radiation intensity field. The figure on the right shows Cases 1–4, and the zoomed view on the left shows the regions for Cases 5 and 6. For each case, the same material parameters are used as those found by matching the simulations using the full radiation push to the experiments, as described in Section 3.3 and listed in Table I.

4. RESULTS

In this section, the results from the six case studies are presented. First, the z-displacement versus time traces for the three points above the inclusion nearest the focus, shown in Figure 7, are plotted to compare the simulation results with the full ARF push to the cases considering the ARF applied to only a subregion of the simulation domain. Figure 8 shows Cases 2–4 compared with considering the full push (Case 1), and Figure 9 shows the results for Cases 5 and 6. In each case, the displacement is normalized by the peak displacement for fair comparison because the pushes on a subregion do not have the same overall force when integrated over the volume. The difference between the full push and threshholding at 99% of the maximum intensity appears small, but all the other results show significant differences, which are discussed further in the next section.

To obtain a bigger view of the excitation on the 3D model, the normalized z-displacement field at approximately 0.5 ms into the dynamic simulation are shown for each case in Figures 10–15 on the right. This is 0.25 ms after the push has ended. The displacement field is normalized by the maximum displacement in each case. The shear wave, which travels through the heterogeneous medium, is also illustrated in the same figures on the imaging plane, which is reversed (right to left) because the imaging plane is on the back side of the model. To illustrate the propagating wave, the normalized z-displacement field on the imaging plane is shown stepped through time from 0.5 to 5 ms for each case study.

DOI: 10.1002/cnm

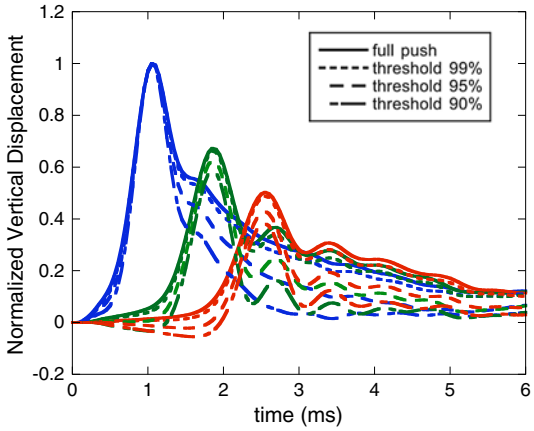

Figure 8. Comparison of the resulting displacement histories between full push and various thresholding cases as a function of time from the finite element simulation, for three points above the inclusion nearest the focus.

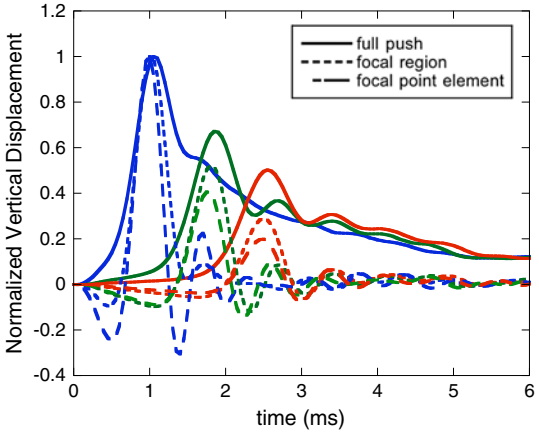

Figure 9. Comparison of the resulting displacement histories between full push and cases including only a push near or at the focus as a function of time from the finite element simulation, for three points above the inclusion nearest the focus.

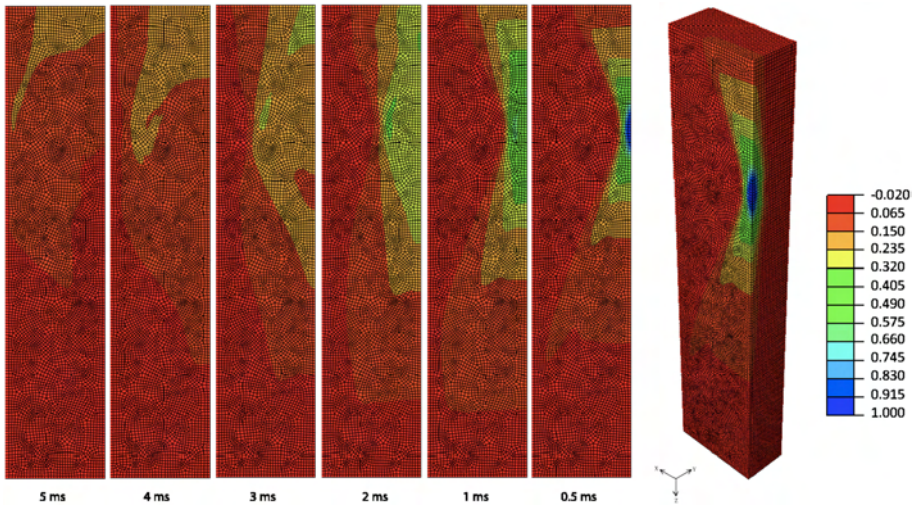

Figure 10. Simulation normalized z-displacement field stepped from 0.5 to 5 ms, full radiation push.

DOI: 10.1002/cnm

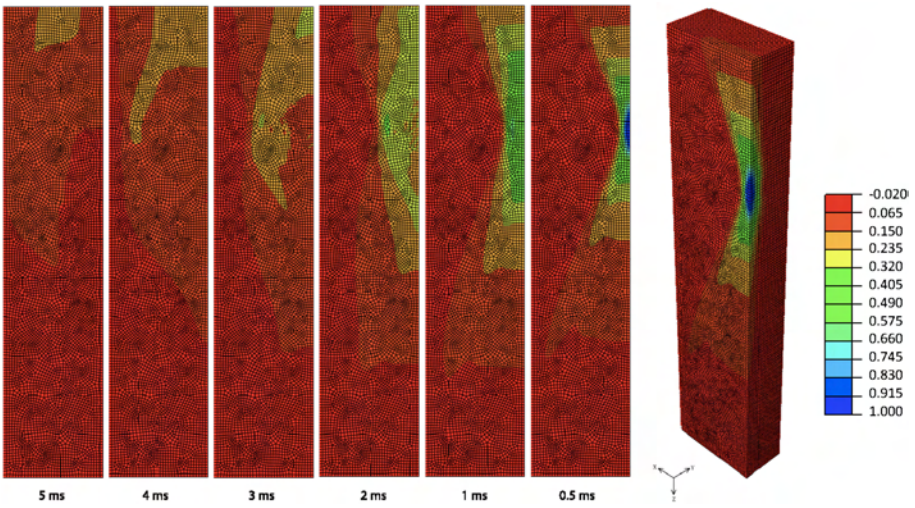

Figure 11. Simulation normalized z-displacement field stepped from 0.5 to 5 ms, threshold at 99%.

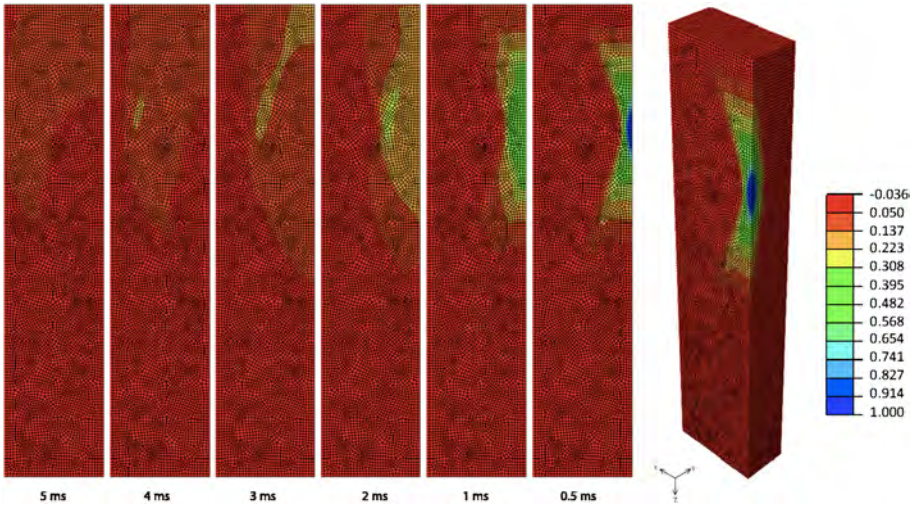

Figure 12. Simulation normalized z-displacement field stepped from 0.5 to 5 ms, threshold at 95%.

5. DISCUSSION

With the results of this work, observations are presented with respect to the accuracy of the finite element model as well as trends from the case studies.

5.1. Model accuracy

From the material properties found by matching the simulations to the experimental data listed in Table I, the frequency dependent shear wave speed and attenuation for a plane wave may be determined. First, the complex shear modulus may be expressed in terms of the angular frequency ω as [26]

$$G^*(\omega) = \mu_0 \left[1 - \sum_{m=1}^{2} g_m \frac{1 - i\omega\tau_m}{1 + \omega^2 \tau_m^2} \right] \tag{23}$$

DOI: 10.1002/cnm

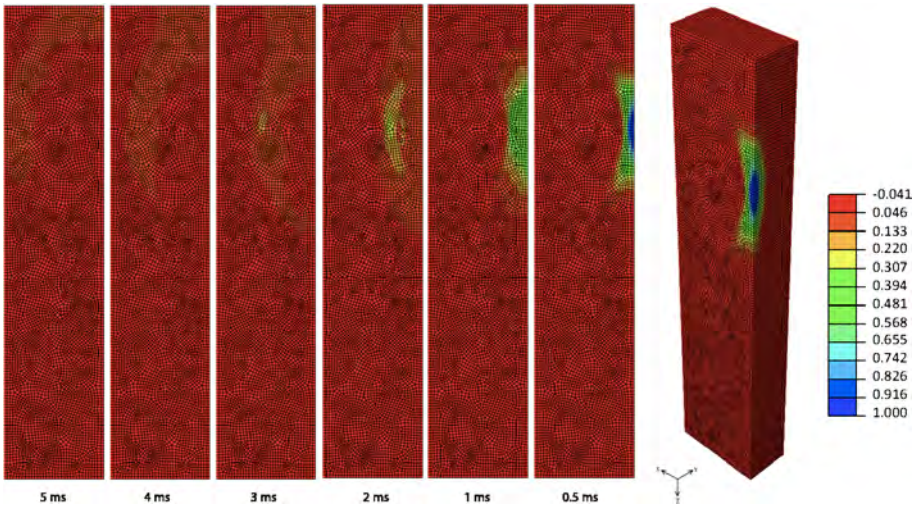

Figure 13. Simulation normalized z-displacement field stepped from 0.5 to 5 ms, threshold at 90%.

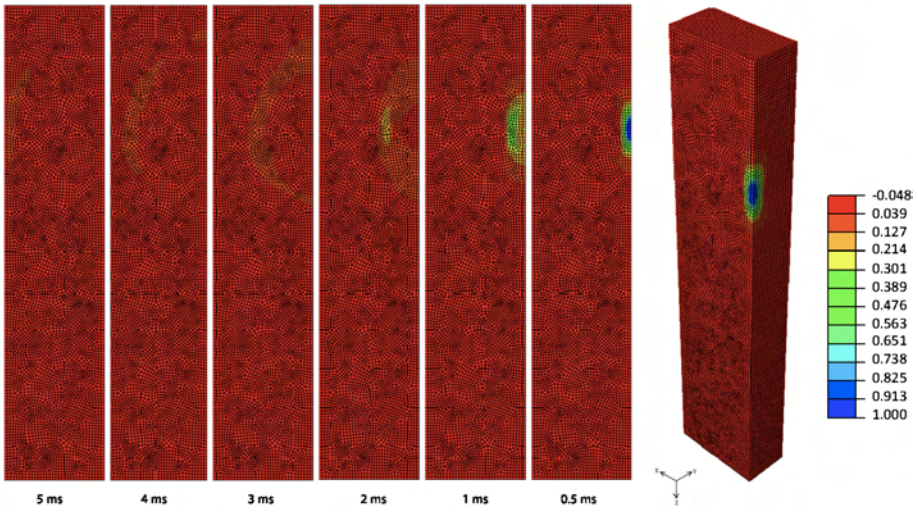

Figure 14. Simulation normalized z-displacement field stepped from 0.5 to 5 ms, focal region push.

Then, the shear wave speed c_s and the shear wave attenuation α_s are

$$c_s = \left[\text{Real}\left(\sqrt{\frac{\rho}{G^*(\omega)}}\right)\right]^{-1} \tag{24}$$

$$\alpha_s = -\omega\left[\text{Imag}\left(\sqrt{\frac{\rho}{G^*(\omega)}}\right)\right] \tag{25}$$

The shear wave speed and attenuation as a function of frequency for the material properties obtained for the background and inclusion are shown in Figure 16(a) and (b).

The high frequency shear wave speeds were selected to match the speed of the wavefronts determined by the arrival times of the wave fronts, leading to a high frequency shear wave speed of 4.3 m/s in the background and 6.6 m/s in the inclusion. The wavefronts in Figures 5 and 6 are fairly well captured as well as the location of the peaks. Thus, the high frequency wave speeds are well represented in the model. Because the excitation is a square pulse for only 250 μs, the dominant frequencies are above 1000 Hz. Therefore, the lower frequency behavior predicted by the model has

DOI: 10.1002/cnm

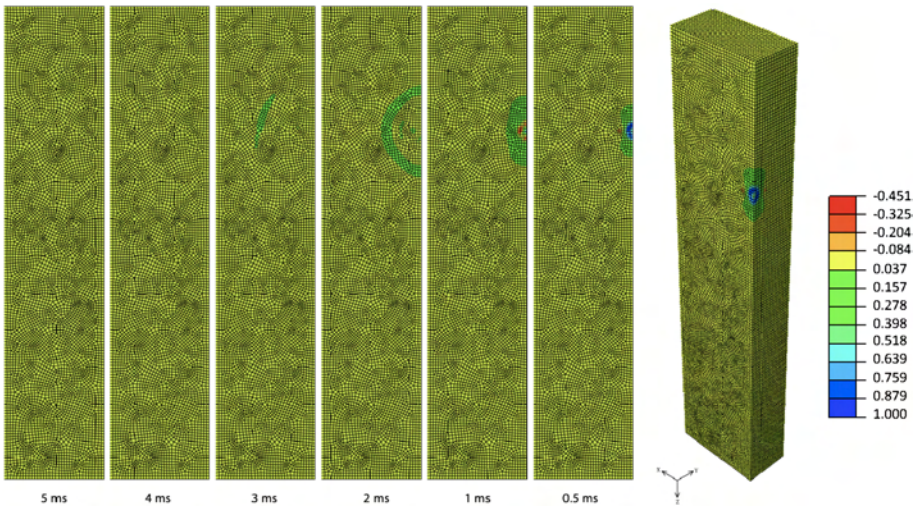

Figure 15. Simulation normalized z-displacement field stepped from 0.5 to 5 ms, point source push.

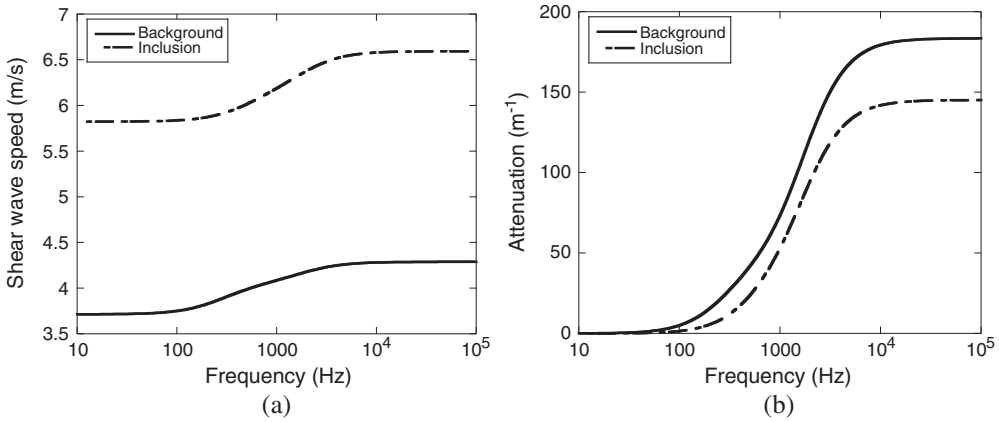

Figure 16. (a) Shear wave speed and (b) attenuation as functions of frequency.

not been tested and may not be valid. Except for the first two peaks, the arrival times and slopes of the displacement curves are very similar to those of the experimental data, both for the points above the inclusion and those passing through the inclusion. The experimental data had a coarser resolution with respect to time, so, it is possible that some peaks were missed in the data, which may be a source in the discrepancy in the first two peaks. In addition, the nodal points in the finite element mesh, where the simulation displacements are computed, were not exactly at the same locations as the points where the experimental data was taken, with a maximum difference in location of 0.12 mm. The attenuation in the peak displacement is also fairly well represented. The peaks for the data points passing through the inclusion were better matched than in the background. On the other hand, the recovery after the peaks is not as well represented by the model. In modifying the material properties, it was difficult to capture both the high attenuation and the shorter tails on the decline after the peak. A higher attenuation in the peaks is characteristic of a more viscous material, whereas the shorter tails implies a more elastic material that recovers more quickly; therefore, the two apparent properties of the experimental data could not easily be modeled. Also, as previously mentioned, the model used in this work was slightly different from the experimental setup to allow for symmetry in the modeling of the body force field. An additional Maxwell element in the model, providing damping at a higher frequency, may improve the match against experimental data by damping out some of the residual oscillations after the peak displacements too, while still

DOI: 10.1002/cnm

allowing for a quick recovery. Finally, for the full radiation push, the displacements at the end of the simulation time are not completely recovered, which is also observed in the experiment (excluding the last data point in the experiment, which was set to zero). However, the lack of recovery to zero in the experimental data may be caused by building noise, in which case, it is not associated with the material response. In the model, it appears that a small reflected wave may be partially responsible for the model displacements not returning to zero by the end of the simulation time.

5.2. Case study observations

Several case studies were performed to determine the effect of utilizing only a percentage of the full radiation push. The use of the full radiation push was the baseline case. Three cases that thresholded the full push to 99%, 95%, and 90% of the maximum body force were investigated to determine the relative displacement accuracy compared with the full push. The last two cases utilized focal region and single element pushes.

By comparing the normalized vertical displacement of selected nodes outside of the focal region as well as the displacement field stepped through time, the effect of using the full radiation push and only a percentage of the full push was observed. In the displacement field images in Figures 10–15, the shear wave front may be observed as it moves from right to left across the imaging plane of the model. Using the full push (Figure 10), as the shear wave passes through the stiffer inclusion, the wave increases in speed, as shown at 3 and 4 ms. As the percentage of the full radiation push decreases from 99% to 90%, the size of the shear wave front decreases, and the attenuation increases. The media also start to recover faster after the peak. Furthermore, the span of the initial displacement field (as shown at 0.5 ms) decreases as the percentage of full push decreases. When only the focal region push is performed, the shear wave front decreases dramatically in size, and the attenuation increases as shown by the decrease in magnitude through time. The media also recover much more quickly, as shown by the distinct wave passing through both the background medium and inclusion. Finally, when the single element point source was implemented, the shear wave front becomes much smaller, the attenuation is highest, and like the focal region push, the media fully recover. It is also interesting to note that when the push is only on a single element (Figure 15), there is a substantial displacement in the upward $-z$ direction (opposite the direction of the push) ahead of the push. This occurs because as the material is locally pushed down at the focus, to preserve volume, the material tends to move upwards in the region next to the push. On the other hand, when the push occurs over a larger region, the material surrounding the focus is subjected to a downward force from material above it, preventing it from moving in the upwards direction. This can be seen more clearly in the displacement plots for distinct points near the focus (Figure 9) discussed next.

When the displacement curves at the distinct points are compared and contrasted for each case, it is evident that the focal region and single element pushes are not adequate to model the effect of using the full radiation push. Figure 9 compares the simulated data from using the full push, focal region push, and single element push. Several observations can be made when using focal region or single element pushes:

- Underdamped displacements, as shown by residual oscillation
- Rapid decrease in displacement after peak
- Narrower peaks
- Full displacement recovery
- Nodes outside the focal region experience initial displacement in opposite direction

As mentioned in [19], the low amplitude of the radiation field plays a significant role in the relaxation time of the response; therefore, the focal region and single element pushes do not match the relaxation of the full radiation and experimental data responses. Based on Figure 9, it is clear that using a focal region or single element point source push is not adequate to accurately model the effects of the entire radiation field.

In addition to investigating the effect of using a focal region or single element point source push, thresholding the full radiation push was evaluated to determine whether reducing the applied force field could produce comparable results with less computation time. Figure 8 compares the simulated

DOI: 10.1002/cnm

data from the full push and the thresholded pushes. These results illustrate that as the threshold percentage decreases, the displacements begin to recover and attenuate more quickly. The initial slope of the curves, and therefore the arrival time of the shear wave, does not significantly vary as the thresholding percentage decreases. Although the figure, coupled with the displacement curves in Section 4 demonstrates that thresholding to a certain degree will not be adequate, it also shows that the 99% threshold is fairly close to the full push displacement. The maximum absolute displacement error between the 99% threshold and the full push in the three selected nodes was less than 4%.

In addition to displacement accuracy, the computation time for the simulations were evaluated to determine if a comparable threshold could reduce the computation time. For Cases 2–6, the simulation time was approximately half that for the full push, which took 66 min to complete on a Lenova T60 with an Intel Core Duo T2500 processor. Because the 99% threshold push utilized approximately 13% of the elements in the full push model and took about 45% of the full push computation time with an absolute displacement error of less than 4%, it may be advantageous to use this threshold in future studies if the error is deemed acceptable.

6. CONCLUSIONS

An approach for modeling in 3D the dynamic displacement response of viscoelastic soft tissue to an ARF from a focused ultrasonic transducer has been presented, and the model is calibrated and compared with experimental data on a tissue-mimicking phantom with a cylindrical inclusion. The radiation intensities were calculated using the pressure field obtained with the Field II software [23], and a variable order Gauss quadrature numerical integration scheme was used to determine the body force for each element in the model, which was proportional to the element intensity. The finite element model was developed in ABAQUS [25]. Owing to a high intensity gradient at the focus, a higher-order integration scheme was used within the focal region to allow for a larger element size while maintaining accuracy, thereby reducing computation time. The viscoelastic material parameters for the background medium and stiffer, cylindrical inclusion were calibrated using a trial-and-error approach by comparing the shear wave response with experimental data. The finite element simulation results matched well with the experimental data with respect to replicating the shear wave speed and attenuation in the peak displacements through the background medium and inclusion, but did not illustrate comparable recovery after the peak displacements.

The focus of this work has been to determine if a focal region or single element point source was adequate to properly model the effects of the full radiation field or if the full field is required. Thresholding the full push has also been investigated to evaluate whether a threshold could produce comparable displacement results, but use less computation time. To accomplish this, several case study simulations were performed using the full radiation push, a focal region push, a single element acting as a point source push, and 99%, 95%, and 90% thresholds of the maximum body force. The displacement fields stepped through time were observed for each case study. Their respective displacement data as a function of time for several nodes across the imaging plane at the focal depth and through the center of the inclusion were compared with experimental data. The simulated displacement data was then compared among the different cases. It was shown that using a focal region or single element push was not sufficient to properly model the effect of the full radiation push and therefore did not match well with the either the simulated data considering the full push nor the experimental data. These pushes produced underdamped, over-attenuated displacements that fully recovered within the simulation time. The produced peaks were also more narrow, and there was an initial displacement in the opposite direction, which was not apparent in the full push and experimental data. With respect to thresholding, the studies showed that a 99% threshold, which ignores the lowest 1% of the body forces, could adequately replicate the full push data within 4% of the absolute displacement, at least for the selected nodes, while reducing the computation time by approximately half.

As a result of this work, a predictive finite element viscoelastic model has been developed, in which the material behavior induced by acoustic radiation force excitation is correlated with experimental data. Because the model has been calibrated to replicate the response from tissue-mimicking

DOI: 10.1002/cnm

phantoms in the experiments; the next step would be to model data obtained from actual tissue samples. In addition to modeling different materials, varied transducer settings may be simulated to determine the effect on the resulting displacement field and shear wave propagation. This model could also be used to test new experimental configurations when the transducer settings, the geometry of the inclusions, or the phantoms are modified. Finally, data from this model may be used to test inverse algorithms to reconstruct the viscoelastic material parameters. For example, the inverse approaches developed by McLaughlin and Renzi [1] as well as Park and Maniatty [2] could be used in conjunction with the model data to test the algorithms and reconstruct the material shear modulus.

ACKNOWLEDGEMENTS

This work has been supported by NIH (5R01AG29804-3) in partnership with the University of Rochester and General Electric Medical Imaging. The authors acknowledge the very useful discussions with J. R. McLaughlin, who suggested this study, and A. Oberai at Rensselaer Polytechnic Institute, as well as C. Hazard at General Electric Global Research, who also developed the software for the experiment.

REFERENCES

1. McLaughlin JR, Renzi D. Using level set based inversion of arrival times to recover shear wavespeed in transient elastography and supersonic imaging. *Inverse Problems* 2006; **22**:707–725. DOI: 10.1088/0266-5611/22/2/019.
2. Park E, Maniatty AM. Finite element formulation for shear modulus reconstruction in transient elastography. *Inverse Problems in Science Engineering* 2009; **17**:605–626. DOI: 10.1080/17415970802358371.
3. Oberai AA, Gokhale NH, Feijoo GR. Solution of inverse problems in elasticity imaging using the adjoint method. *Inverse Problems* 2003; **19**:297–313.
4. Ophir J, Céspedes I, Ponnekanti H, Yazdi Y, Li X. Elastography: A quantitative method for imaging the elasticity of biological tissues. *Ultrasonic Imaging* 1991; **13**:111–134.
5. Sarvazyan AP, Rudenko OV, Swanson SD, Fowlkes JB, Emelianov SY. Shear wave elasticity imaging: A new ultrasonic technology of medical diagnostics. *Ultrasound in Medicine and Biology* 1998; **24**:1419–1435.
6. Sandrin L, Tanter M, Catheline S, Fink M. Shear modulus imaging with 2-D transient elastography. *IEEE Transactions on Ultrasonics, Ferroelectrics, and Frequency Control* 2002; **49**:426–435.
7. Nightingale KR, Palmeri ML, Nightingale RW, Trahey G. On the feasibility of remote palpation using acoustic radiation force. *Journal of the Acoustical Society of America* 2001; **110**:625–634. DOI: 10.1121/1.1378344.
8. Taylor LS, Porter BC, Rubens DJ, Parker KJ. Three-dimensional sonoelastography: Principles and practices. *Physics in Medicine and Biology* 2000; **45**:1477–1494.
9. Muthupillai R, Lomas DJ, Rossman PJ, Greenleaf JF, Manduca A, Ehman RL. Magnetic resonance elastography by direct visualization of propagating acoustic strain waves. *Science* 1995; **269**:1854–1857.
10. Lizzi F, Muratore R, Deng CX, Ketterling J, Alam K, Mikaelian S, Kalisz A. Radiation-force technique to monitor lesions during ultrasound therapy. *Ultrasound in Medicine and Biology* 2003; **29**:1593–1605. DOI: 10.1016/S0301-5629(03)01052-4.
11. Sack I, Beierbach B, Wuerfel J, Klatt D, Hamhaber U, Papazoglou S, Martus P, Braun J. The impact of aging and gender on brain viscoelasticity. *NeuroImage* 2009; **46**:652–657. DOI: 10.1016/j.neuroimage.2009.02.040.
12. Catheline S, Thomas J, Wu F, Fink M. Diffraction field of a low frequency vibrator in soft tissues using transient elastography. *IEEE Transactions on Ultrasonics, Ferroelectrics, and Frequency Control* 1999; **46**:1013–1019.
13. Bercoff J, Tanter M, Fink M. Supersonic shear imaging: A new technique for soft tissue elasticity imaging. *IEEE Transactions on Ultrasonics, Ferroelectrics, and Frequency Control* 2004; **51**:396–409.
14. Nightingale K, McAleavey S, Trahey G. Shear-wave generation using acoustic radiation force: *In vivo* and *ex vivo* results. *Ultrasound in Medicine and Biology* 2003; **29**:1715–1723. DOI: 10.1016/j.ultrasmedbio.2003.08.008.
15. Chen S, Urban MW, Pislaru C, Kinnick R, Zheng Y, Yao A, Greenleaf JF. Shearwave dispersion ultrasound vibrometry (SDUV) for measuring tissue elasticity and viscosity. *IEEE Transactions on Ultrasonics, Ferroelectrics, and Frequency Control* 2009; **56**:55–62. DOI: 10.1109/TUFFC.2009.1005.
16. Wu Z, Taylor LS, Rubens DJ, Parker KJ. Sonoelastic imaging of interference patterns for estimation of the shear velocity of homogeneous biomaterials. *Physics in Medicine and Biology* 2004; **49**:911–922. DOI: 10.1121/1.2203594.
17. Lin K, Mclaughlin J, Thomas A, Parker K, Castaneda B, Rubens D. Two-dimensional shear wave speed and crawling wave speed recoveries from *in vitro* prostate data. *Journal of Acoustical Society of America* 2011; **130**:585–598. DOI: 10.1121/1.3596472.
18. Hah Z, Hazard C, Cho YT, Rubens D, Parker K. Crawling waves from radiation force excitation. *Ultrasonic Imaging* 2010; **32**(2010):177-189.

19. Bercoff J, Tanter M, Muller M, Fink M. The role of viscosity in the impulse diffraction field of elastic waves induced by the acoustic radiation force. *IEEE Transactions on Ultrasonics, Ferroelectrics, and Frequency Control* 2004; **51**:1523–1536.
20. Palmeri ML, Sharma AC, Bouchard RR, Nightingale RW, Nightingale KR. A finite-element method model of soft tissue response to impulsive acoustic radiation force. *IEEE Transactions on Ultrasonics, Ferroelectrics, and Frequency Control* 2005; **52**:1699–1712.
21. Vappou J, Maleke C, Konofagou EE. Quantitative viscoelastic parameters measured by harmonic motion imaging. *Physics in Medicine and Biology* 2009; **54**:3579–3594. DOI: 10.1088/0031-9155/54/11/020.
22. Giannoula A, Cobbold RSC. Image reconstruction of local shear and viscosity moduli for a finite-amplitude acoustic modulated radiation force. *2009 IEEE Ultrasonics Symposium*; 1887–1890.
23. Jensen JA. Field: A program for simulating ultrasound systems. In *the 10th Nordic-Baltic Conference on Biomedical Imaging Published in Medical and Biological Engineering and Computing*, Vol. 34, 1996; 351–353, Supplement 1, Part 1.
24. Jensen JA, Svendsen NB. Calculation of pressure fields from arbitrarily shaped, apodized, and excited ultrasound transducers. *IEEE Transactions on Ultrasonics, Ferroelectrics, and Frequency Control* 1992; **39**:262–267.
25. *Abaqus Theory Manual, Version 6.10*, Dassault Systemes Simulia Corp. Providence, RI, 2010.
26. Fung YC. *Foundations of Solid Mechanics*. Prentice-Hall: New Jersey, 1965.
27. Fung YC. *Biomechanics: Mechanical Properties of Living Tissue*, 2nd edn. Springer-Verlag: New York, 1993.
28. Bower AF. *Applied Mechanics of Solids*. Taylor & Francis Group: Boca Raton, FL, 2010.
29. Gooberman GL. *Ultrasonics: Theory and Application*. The English Universities Press, LTD: London, 1968.
30. Edmonds PD (ed.). *Ultrasonics*, Methods of Experimental Physics, Vol. 19. Academic Press: New York, 1981.
31. Dyer CC, Ip PSS. Gaussian quadrature, An elementary introduction to scientific computing, (2002, Apr.) [Online]. Available: http://pathfinder.scar.utoronto.ca/dyer/csca57/bookP/node44.html. Date Last Accessed 04/21/2011.
32. Hughes TJR. *The Finite Element Method: Linear Static and Dynamic Finite Element Analysis*. Dover Publications, Inc.: Mineola, New York, 2000.
33. Cohen M, Jennings PC. Silent boundary methods for transient analysis. In *Computational Methods for Transient Analysis*, Belytschko T, Hughes TJR (eds). North-Holland: New York, 1983; 301–360.